On the Shoaling of Solitary Waves in the Presence of Short Random Waves

MIAO TIAN AND ALEX SHEREMET

Department of Civil and Coastal Engineering, University of Florida, Gainesville, Florida

JAMES M. KAIHATU

Zachry Department of Civil Engineering, Texas A&M University, College Station, Texas

GANGFENG MA

Department of Civil and Environmental Engineering, Old Dominion University, Norfolk, Virginia

(Manuscript received 12 July 2014, in final form 2 December 2014)

ABSTRACT

Overhead video from a small number of laboratory tests conducted by Kaihatu et al. at the Tsunami Wave Basin at Oregon State University shows that the breaking point of a shoaling solitary wave shifts to deeper water if random waves are present. The analysis of the laboratory data collected confirms that solitary waves indeed tend to break earlier in the presence of random wave field, and suggests that the effect is the result of the radiation stresses gradient induced by the random wave fields. A theoretical approach based on the forced KdV equation is shown to successfully predict the shoaling process of the solitary wave. An ensemble of tests simulated using a state-of-the-art nonhydrostatic model is used to test the statistical significance of the process. The results of this study point to a potentially significant oceanographic process that has so far been ignored and suggest that systematic research into the interaction between tsunami waves and the swell background could increase the accuracy of tsunami forecasting.

1. Introduction

The solitary wave has long been the working paradigm for both experimental and numerical simulations of tsunamis (e.g., Ippen and Kulin 1954), persisting as the common performance benchmark for numerical models (e.g., Madsen et al. 2008; Ma et al. 2012; Grilli et al. 2002; and many others) even after the emergence of more realistic models that account, for example, for "N-waves" (Tadepalli and Synolakis 1994) and solitary wave fission (i.e., the disintegration of a leading wave into a train of solitary waves; Madsen and Mei 1969). Because tsunamis reach deep-water phase speeds of the order of 200 m s^{-1} (Geist et al. 2006) and flow velocities near 2–5 m s^{-1} when impacting the coast (Fritz et al. 2012), the term "solitary" was also used in the "soliton" sense—implying a general insensitivity to the oceanographic and sedimentary background. Nevertheless, the need for more realistic forecasting models has eventually encouraged efforts to include the effects of the oceanographic background. Recent studies have considered tsunami interaction with tides (Kowalik et al. 2006) and vorticity (Constantin and Johnson 2008), as well as more accurate and realistic initial conditions needed to better reproduce tsunami fission (Matsuyama et al. 2007).

In accordance with the soliton paradigm, the interaction between tsunamis and wind-wave fields has been approximated as affecting only the wind waves (e.g., Longuet-Higgins 1987; Zhang and Melville 1990). As a slowly varying current, the tsunami can force wave steepening, a description that applies for a scale separation between the current and wave of the order $\gamma = O(\mu^{3/2})$, where γ is the ratio of the characteristic spatial scales and μ is the wave steepness. In deep water, the soliton paradigm is justified by the significant scale separation (100 m to 100 km; 10 to 200 m s^{-1}) as well as the intrinsic stability of the soliton as a coherent structure (Osborne 2010).

In the nearshore, however, it is conceivable that the effect of the wind-wave fields on the tsunami could

Corresponding author address: Miao Tian, Department of Civil and Coastal Engineering, University of Florida, 365 Weil Hall, Gainesville, FL 32611.
E-mail: mtian04.18@ufl.edu

DOI: 10.1175/JPO-D-14-0142.1

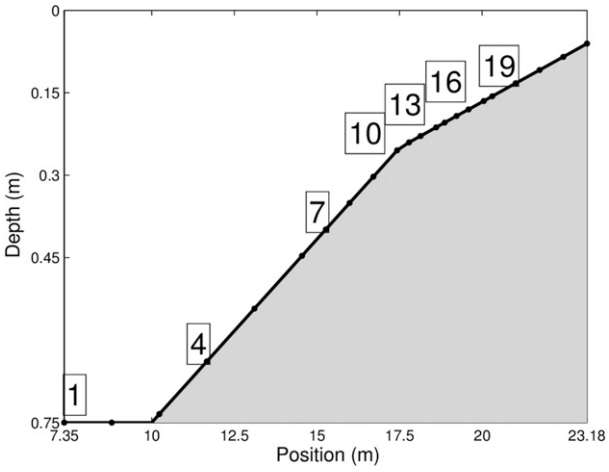

FIG. 1. Bathymetry profile of the experiment. Representative sensors are highlighted using text boxes.

become significant as the characteristic length and speed of the tsunami decrease. From the point of view of soliton dynamics, the balance between dispersion and nonlinearity is broken, with the solitary wave eventually breaking in shallow water. Field observations (e.g., Aida et al. 1964; Madsen et al. 2008) and numerical simulations (e.g., Madsen et al. 2008) also show that the scale gap between the tsunami and wind waves decreases significantly even for relatively short swells. For example, the 2004 Indian Ocean tsunami in the Strait of Malacca had a height of 5 m in 14-m water depth (Madsen et al. 2008); the assumption of a KdV solitary wave shape yields a characteristic length of 240 m (based on Goring 1979). For 10-s, 2-m swell waves, one obtains $\gamma \sim O(\mu^{1/2})$, that is, $\gamma = 0.375$ with $\mu = 0.14$. This suggests that more complicated interactions may occur in the nearshore that cannot be reduced to the above wave–current interaction paradigm.

The possibility of nontrivial interactions between tsunamis and background swell over a sloping bathymetry in shallow water (at swell scale) was investigated in a series of laboratory experiments by Kaihatu and El Safty (2011) and Kaihatu et al. (2012). Remarkably, images recorded by overhead cameras observing a solitary wave shoaling over a random wave field suggest that background waves can accelerate the solitary wave-breaking process. Using wavelet analysis, Kaihatu and El Safty (2011) showed that the energy of the short-wave band increased when the solitary wave and the random wave field were superposed. While this process may be connected to the acceleration of breaking seen in the overhead imagery, the interaction mechanism forcing the early breaking is not understood. Although the phenomenon was observed in the laboratory (with all the implied scaling limitations when representing tsunami dynamics), understanding the mechanism responsible for the wave–tsunami coupling could be important for improving tsunami forecasting skill of models as well as their interaction with other aspects of the environment (e.g., sediment and sediment transport).

TABLE 1. Wave parameters for short random waves, where H_s is the significant wave height, T_p is the peak period, kh is the relative depth, a/h is the nonlinearity, and Ur is the Ursell number.

Run	H_s (m)	T_p (s)	$(kh)^2$	a/h	Ur
W1	0.1	2	1	0.067	0.067
W2	0.05	4	0.02	0.033	0.163
W3	0.2	2	1	0.134	0.134
W4	0.1	4	0.02	0.067	0.331

This study focuses on the analysis of the experimental data (described in section 2) in an attempt to identify the location of the initial breaking event and evaluate possible mechanisms for tsunami–swell interaction (section 3). The results are validated numerically in section 4 and summarized in section 5, where the future directions of research are also discussed.

2. Observations and data analysis

a. Laboratory experiment

The laboratory experiment was conducted during March 2010 at the Tsunami Wave Basin (48.8 m long, 26.5 m wide, and 2.1 m deep) at Oregon State University. Details of the experiment are given in Kaihatu and El Safty (2011) and Kaihatu et al. (2012). The bathymetry profile (Fig. 1) was piecewise linear, with a 0.75-m depth flat section for $0\,\text{m} \le x \le 10\,\text{m}$, a slope of $1/15$ for $10\,\text{m} \le x \le 17.5\,\text{m}$, and a slope of $1/30$ for $17.5\,\text{m} \le x \le 25\,\text{m}$ (x is the cross-shore coordinate, with the origin at the location of the wave maker). Free-surface elevation data were collected at a sampling rate of 50 Hz at 22 locations from $x = 7.35\,\text{m}$ to $x = 23.18\,\text{m}$ using wire resistance sensors. Overhead video imagery was also recorded from two web cameras.

The experiment performed four tests (runs W1 to W4 in Table 1) with the same solitary wave shoaling alternatively over undisturbed water (run S) and random wave fields (runs SW1 to SW4). The random waves were generated based on a Texel–Marsden–Arsloe (TMA) spectrum (Bouws et al. 1985) using default values for the free parameters for spectral shape. Intrinsic constraints in the mechanics of generating solitary waves in the laboratory, as well as strong seiching resulting from the solitary wave runup, limited the duration of runs that included the solitary waves to 4 min. However, 6- and 12-min runs of each of the four random wave conditions with and without a solitary wave were also recorded

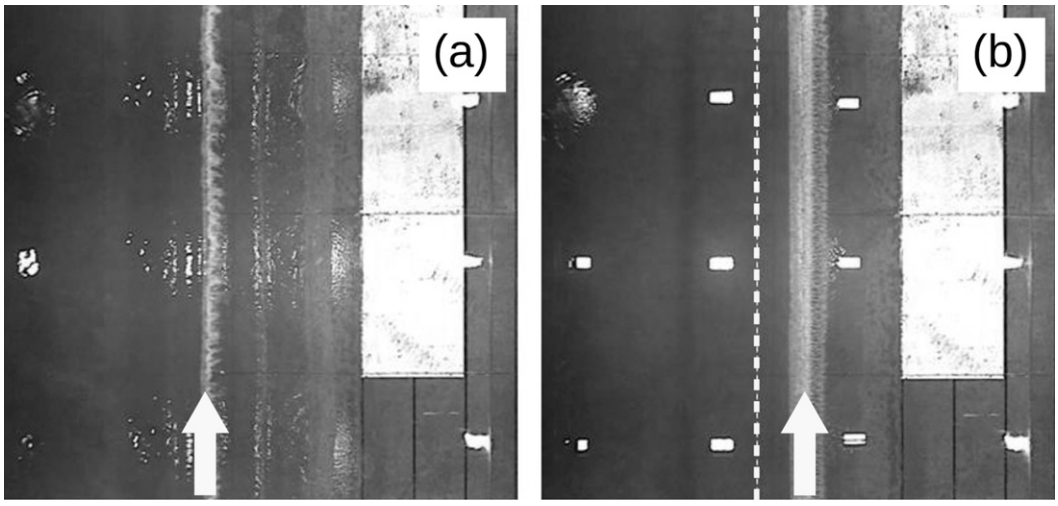

FIG. 2. Frames from overhead video showing the location of the breaking point of the solitary wave propagating (a) in the presence of random waves and (b) over still water. The arrow marks the approximate location of the breaking point in each frame. The location of the dashed line in (b) corresponds to the location of the breaking point (arrow) in (a).

separately (runs SW1 to SW4 and W1 to W4) to allow for statistical analysis.

The characteristics of the random wave fields were chosen to preserve the values of nondimensional parameters important for reproducing prototype processes (Table 1). The nonlinearity of the solitary wave ($a_s/h = 0.33$, where a_s is the solitary wave amplitude and h is the characteristic depth) corresponds to a tsunami of 5-m amplitude in 14-m water depth (e.g., the 2004 Indian Ocean tsunami in the Strait of Malacca; Madsen et al. 2008). The random wave tests include two runs (W1 and W3) with dispersive waves characterized by $(kh)^2 \simeq 1$, where k is the characteristic wavenumber, and two weakly dispersive runs (W2 and W4) with $(kh)^2 \simeq 0.02$. Ursell numbers for the runs range between 0.067 (W1, weakly nonlinear) and 0.33 (W4, strongly nonlinear).

The analysis presented here is motivated by Fig. 2. A careful comparison of the overhead video of the solitary wave alone and in the presence of random waves seems to indicate that random waves accelerate the solitary wave-breaking process (Kaihatu and El Safty 2011). However, the interpretation of the images in Fig. 2 is subjective, and the exact moment of breaking depends on the type of breaking process and the definition of the instantaneous breaking event.

Time series from the experiment (e.g., Fig. 3) suggest that the transformation of the solitary wave in all runs is characterized by the peaking and steepening of the wave front, similar to plunging breakers in random waves (e.g., Whitham 1974; Peregrine 1983; confirmed by visual inspection at the site). However, because the

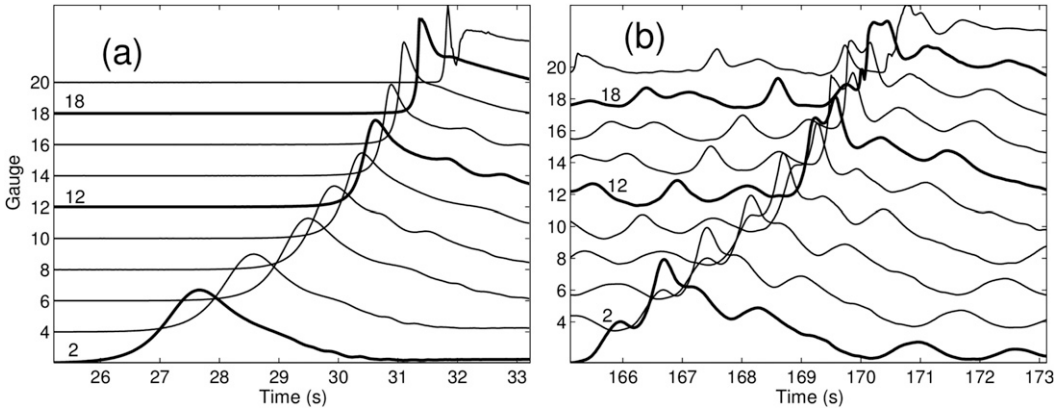

FIG. 3. Surface elevation (arbitrary units) for every two sensors from sensor 2 to sensor 20 for (a) run S and (b) run SW1. Thick lines indicate sensors 2, 12, and18; thin lines indicate the rest of the sensors.

instruments cannot detect a vertical surface corresponding to a vertical wave front, a weaker breaking criterion is needed based on observing the overall evolution of the frontal steepness.

Therefore, the breaking point is defined here as the position of the maximum frontal slope; this is also used by Kaihatu and El Safty (2011) and Kaihatu et al. (2012) in their analysis of the wave evolution characteristics of these experiments. This definition is subject to the ambiguity of defining the wave slope itself; therefore, it seems prudent to use several slope definitions and derive conclusions based on the consistency of the results.

b. Analysis methods

1) Energy flux estimate

The evolution of energy flux associated with the solitary wave and the random wave field can be used to identify possible nonlinear interactions between them. The energy flux for a potential flow is (e.g., Mei et al. 2005)

$$F = \rho \frac{1}{T} \int_{t_0}^{t_0+T} \int_{-h}^{\eta} \phi_t \phi_x \, dz \, dt, \tag{1}$$

where T is a characteristic time, ϕ is the velocity potential, x is the wave propagation direction, and ρ is the density. Equation (1) can be approximated based on the information about the free-surface elevation η. For random waves, the energy flux of short random waves was estimated using the linear approximation in discrete form:

$$F = \frac{\rho g}{2} \sum_{j}^{n} |a_j|^2 C_j, \tag{2}$$

where ω_j, k_j, and C_j are the radian frequency, wavenumber, and group velocity of the spectral mode j; a_j is the complex amplitude of mode j in the Fourier decomposition of the free-surface η; and n is the total mode number and h is the local depth.

The solitary wave is assumed to have negligible dependence on the vertical coordinate. Equation (1) then simplifies to

$$F = \rho g \frac{1}{T} \int_{t_0}^{t_0+T} u\eta(\eta + h) \, dt, \quad u = \frac{c\eta}{h}, \quad c = \sqrt{g(h+a)}, \tag{3}$$

where nonlinear effects at breaking are accounted for, and a and c are the amplitude and phase velocity of the solitary wave.

2) Frontal steepness

The wave steepness is defined by the spatial gradient of the free-surface elevation. Observations based on stationary wave gauges, however, are time series at fixed locations: $\eta(x, t)$. The spatial slope η_x can be related to the time derivative η_t using the linear approximation $\eta_t = -c\eta_x$, (e.g., Kaihatu and El Safty 2011; $c = \sqrt{gh}$, with h as the local depth and g as the gravitational acceleration). Because nonlinear behavior is expected to dominate near the breaking point, a KdV approximation (e.g., Whitham 1974),

$$\eta_t + c\left(1 + \frac{3\eta}{2h}\right)\eta_x + \gamma\eta_{xxx} = 0, \quad c = \sqrt{gh}, \quad \gamma = \frac{1}{6}ch^2, \tag{4}$$

may be more appropriate (e.g., $h = 0.75$ m, where $a_s = 0.25$ m yields $a_s/h \simeq 0.33$). Breaking occurs in shallow water, where the dispersive term should be less important. Indeed, typical experimental values of $a_s = 0.25$ m and $L = 10$ m (based on Goring 1979) yield an Ursell number

$$\frac{\frac{3}{2}\frac{c}{h}\eta\eta_x}{\gamma\eta_{xxx}} \sim \mathrm{Ur} = \frac{a_S}{h}\frac{L^2}{h^2} = 10^3 \gg 1, \tag{5}$$

suggesting that the nonlinear term dominates. Neglecting the dispersive term in Eq. (4) yields for the wave steepness the nonlinear relation

$$\eta_x = -\left[\sqrt{gh}\left(1 + \frac{3\eta}{2h}\right)\right]^{-1}\eta_t. \tag{6}$$

The slope $\eta_x^{(S)}$ of the solitary wave elevation $\eta^{(S)}$ can be used to define two estimates of the breaking point, based on the location of the maximum steepness or the maximum mean steepness. The maximum frontal steepness is simply the maximum value of the frontal steepness recorded: $[\eta_x^{(S)}]_{\max} = \sup_{x,t}\eta_x^{(S)}$. The maximum mean steepness is the maximum ratio of the solitary wave amplitude to the horizontal span L_F of the front $\langle\eta_x^{(S)}\rangle_{\max} = \sup_x(a_S/L_F)$, where sup represents the max function.

3) Wavelet filtering

One of the basic difficulties in comparing observations of the solitary wave alone and in the presence of random wave fields is separating the two wave structures. This is especially true for estimating the steepness of the solitary wave as the superposed waves distort the solitary wave surface (Fig. 3b). Filtering out the random wave signal becomes necessary, but simple

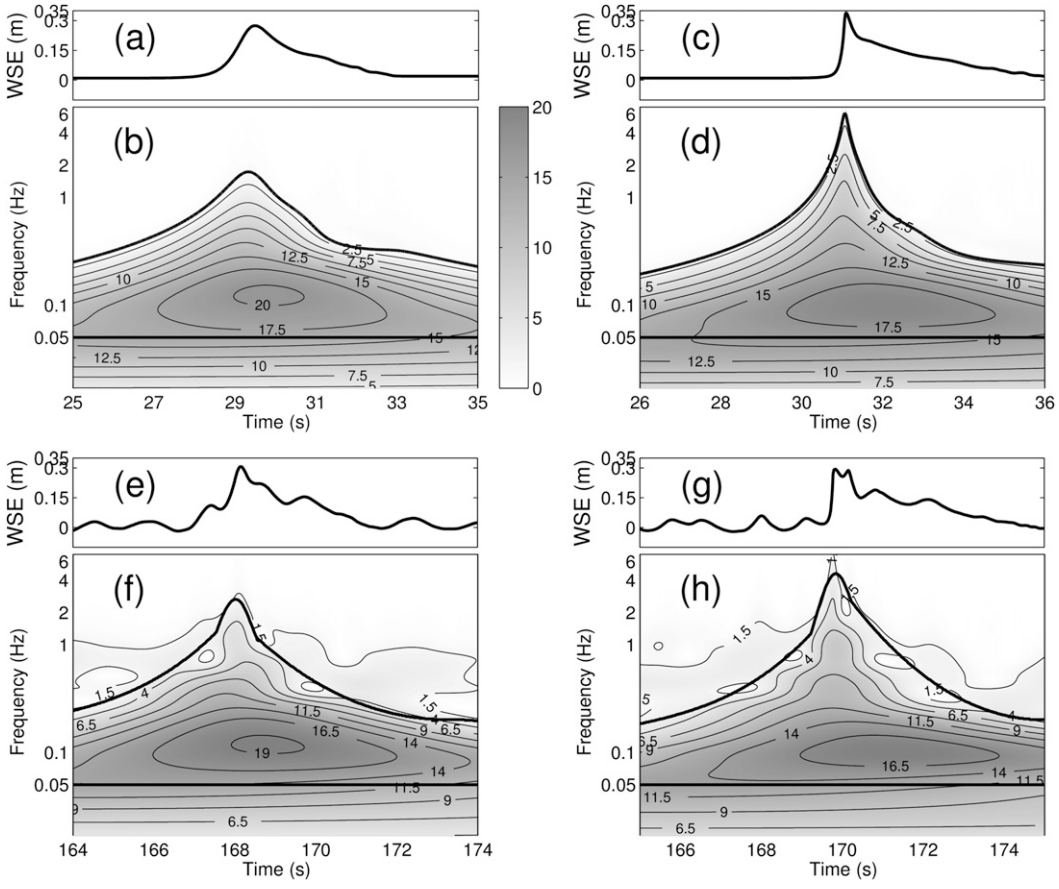

FIG. 4. (a),(c),(e),(g) Time series and (b),(d),(f),(h) wavelet scalogram for (top) run S and (bottom) run SW1. Scalograms shown for (left) sensor 6 and (right) sensor 16. The thick black contour lines Γ_S and Γ_{SW} are used for the filtering procedure (see text for details).

frequency filters (e.g., a Fourier filter) are not usable because they do not differentiate between the random wave signal and the bound high-frequency components associated with the steep frontal slope of the solitary wave. The approach used here takes advantage of the intrinsic temporal localization of the solitary wave and uses time–frequency analysis (e.g., wavelet transforms; see Chui 1992; Torrence and Compo 1998; and many others). Time localization allows for separating at least the nonsynchronous, random wave, high-frequency Fourier components from the bound components associated with the solitary wave-breaking process.

The continuous wavelet transform pair is defined as a two-parameter (s, τ) transformation:

$$G(s,\tau) = \int_{-\infty}^{\infty} g(t)\Psi^*_{s,\tau}\left(\frac{t-\tau}{s}\right) dt, \quad \text{and} \tag{7}$$

$$g(t) = N_\Psi^{-1} \int_{-\infty}^{\infty}\int_{-\infty}^{\infty} G(s,\tau)\Psi_{s,\tau}(t)\, d\tau\, ds, \tag{8}$$

where g and G are the transform pair of functions, and Ψ is the mother wavelet (here, Morlet wavelet; see Goupillaud et al. 1984)

$$\Psi(t) = \pi^{-1/4} \exp\left(-\frac{t^2}{2}\right) \exp(i\omega_0 t), \tag{9}$$

with $\omega_0 = 3$ (Farge 1992). The coefficient N_Ψ is the norm of the mother wavelet Ψ. The parameters τ and s represent the translation and scaling groups of transformations. The quantity $|G|^2$ is called the scalogram. The wavelet transform of Eqs. (7)–(8) conserves the energy of the signal in the sense that $\int |G|^2\, d\tau\, ds = \int |g(t)|^2\, dt$.

Figure 4 shows examples of scalograms for runs S and SW1 at sensors 6 and 16. The solitary wave scalogram has a pyramidal shape (Figs. 4b,d), obvious also when random waves are present, and which becomes vertically elongated and sharp (high-frequency components; Figs. 4b–d) before breaking. Here, the solitary wave signal $g_S(t)$ is identified by inverting only the

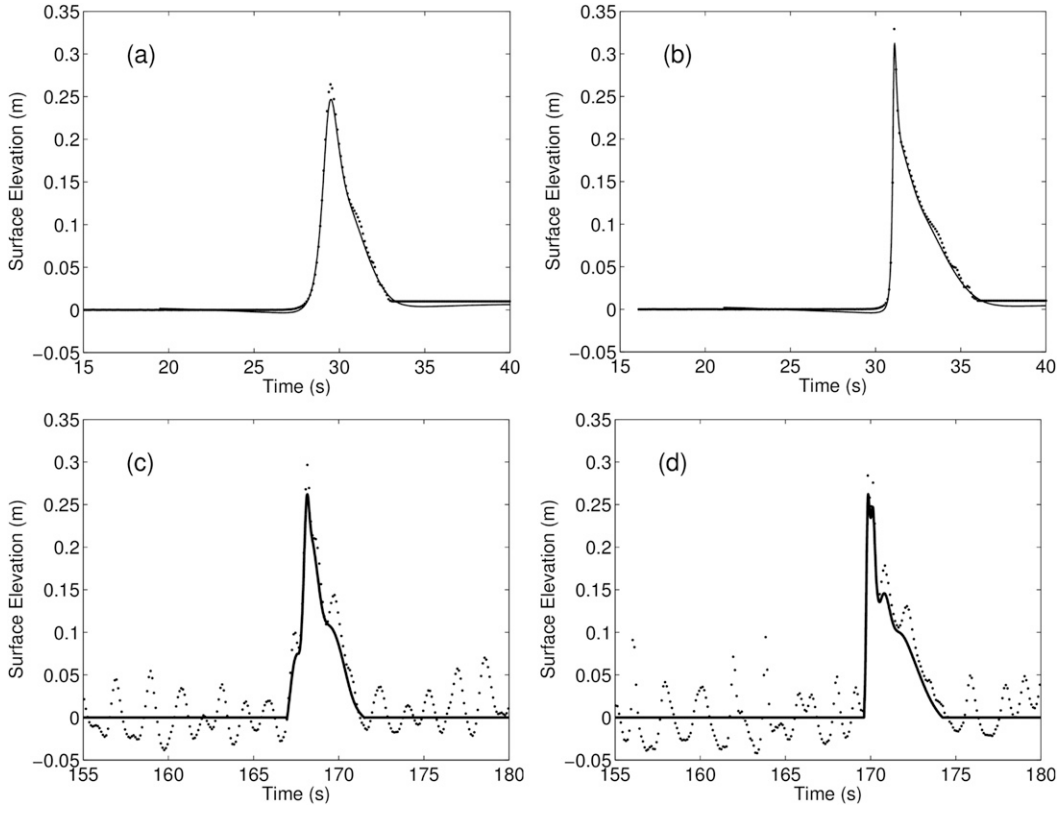

FIG. 5. Comparison between the original (dots) and wavelet filtered time series (lines), for (a),(b) run S and (c),(d) run SW1 at (left) sensor 6 and (right) sensor 16.

scalogram region inside the pyramidal shape, that is, by determining in the time–frequency space a closed contour Γ that defines the solitary wave ''pyramid'' and computing

$$g(t) = N_{\Psi}^{-1} \int_{-\infty}^{\infty} \int_{-\infty}^{\infty} G(s,\tau)\, \chi \Psi_{s,x}(t)\, d\tau\, ds,$$

$$\chi(s,\tau) = \begin{cases} 1 & \text{inside } \Gamma, \\ 0 & \text{otherwise}. \end{cases}$$

where χ is the characteristic function of the pyramid. This procedure does not eliminate the random wave variance inside the pyramid. The exact determination of the contour Γ is rather arbitrary. Here, Γ was defined by choosing a closed scalogram contour (some smoothing was necessary) enclosing 98% of the variance in the Δt segment, that is,

$$\oint_{\Gamma} |G|^2\, d\tau\, ds = 0.98 \int_{t}^{t+\Delta t} dt \int ds |G|^2, \qquad (10)$$

where $\Delta t = 6$ s represents the effective duration of the solitary wave (Goring 1979). Similar to the edge effect of the Fourier transform, the cone of influence occurs at the beginning and end of the wavelet scalograms because we deal with time series with finite length. This effect was minimized by zero padding the time series up to $N = 1024$ points. The wavelet transform was performed by using the wavelet script for MATLAB developed by Torrence and Compo (1998). The procedure reconstructs well the original solitary wave for run S (Figs. 5a,b). For the SW1 case, the wavelet filter captures the sharp peak of the solitary wave and preserves the slope of the wave front (Figs. 5c,d). To conclude this discussion, the validity of the method used here hinges on a significant frequency separation between solitary wave and the random wave field, which appears to be satisfied in this case.

3. Results

a. *Solitary wave shoaling and breaking*

Figure 6 shows the evolution of the solitary wave frontal steepness. For all runs, and regardless of the steepness estimator used (linear or nonlinear, maximum or mean), the evolution of the solitary wave frontal steepness (Fig. 6) shows two maxima, suggesting two individual breaking events. In run S (solitary wave alone), breaking events are sharp and occur in close

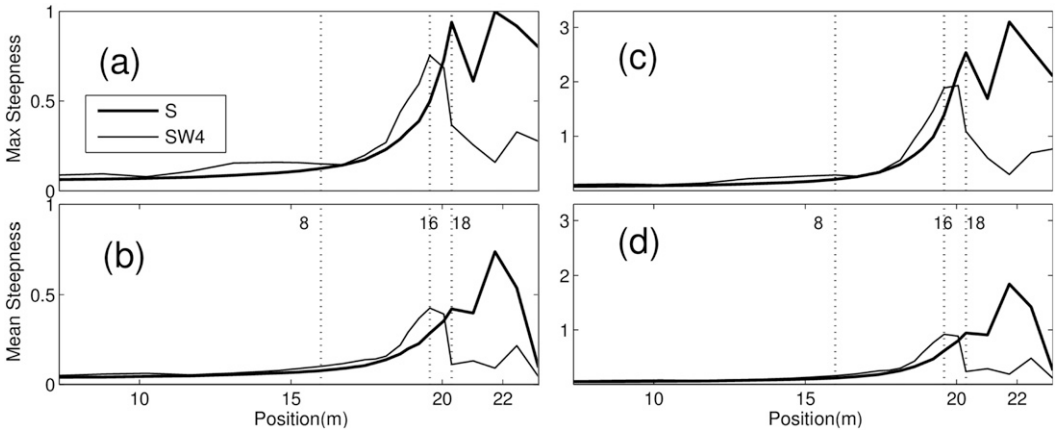

FIG. 6. Evolution of the frontal steepness in runs S and SW4. (a),(b) Nonlinear and (c),(d) linear steepness estimates. (top) The maximum steepness and (bottom) the mean steepness. Thick lines refer to run S; thin lines refer to run SW4. All four runs show similar trends. Dashed lines mark breaking locations.

succession at sensors 18 and 20. This is in marked contrast with the evolution in the presence of random waves, as seen in run SW4, illustrated in Fig. 6. All SW runs behaved similar to SW4 (with the exception of SW3, in which the solitary wave breaks at sensor 8). In the presence of waves (Fig. 6), the first breaking event is ''smoother,'' with a milder slope (sensor 16), while the second breaking is much weaker and occurs farther onshore (sensor 21). Steepness values grow faster for SW4 than for S before the maximum but stay much lower after that. Overall, the trends of the steepness estimators seem to agree with assertion derived from visual observation (Fig. 2) that the solitary wave breaks earlier in the presence of random waves.

Wave–amplitude evolution (Fig. 7) is not exhibited as a clear indication of the early breaking of the solitary wave in the SW runs. In both S and SW runs, the amplitude peaks at sensor 20, with the exception, again, of the SW3 run. However, there is a subtle difference: for evolution in the presence of random waves, the growth rate of the solitary wave amplitude is noticeably weaker, especially close to the breaking point (SW1 and SW3 show almost no growth; Fig. 7c). This behavior suggests a difference in the mechanisms leading to the solitary wave breaking in the runs S and SW. Alone (run S), the solitary wave appears to break by growing and peaking, much like a regular shoaling wave. In the presence of random waves, the frontal slope grows faster, but the amplitude growth is suppressed.

Random waves clearly have an effect on the solitary wave, but the mechanism for interaction is not clear. Possible nonlinear interactions should have an

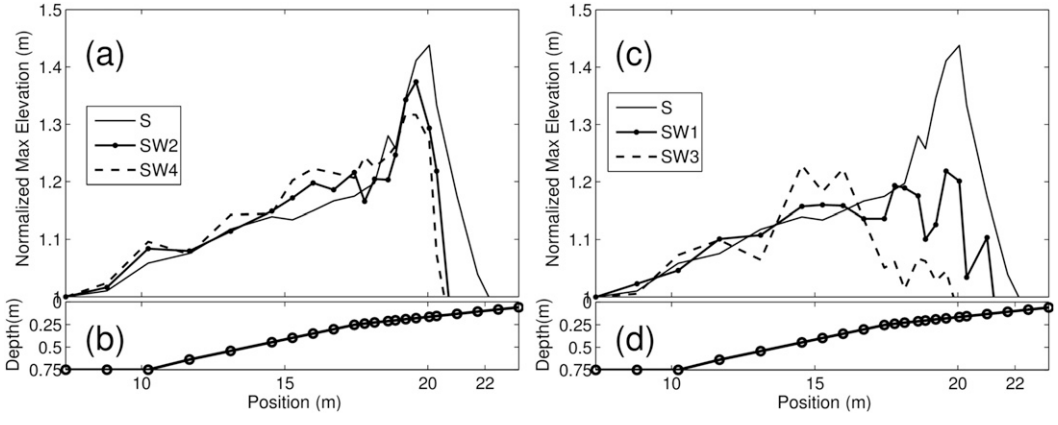

FIG. 7. Solitary wave amplitude (obtained from the wavelet-filtered time series) as a function of position. (a),(c) Evolution of solitary wave amplitude normalized by the initial value; (b),(d) bathymetry with the location of the sensors. Solid lines indicate the solitary wave, dotted lines indicate runs SW1 and SW2, and dashed lines indicate runs SW3 and SW4.

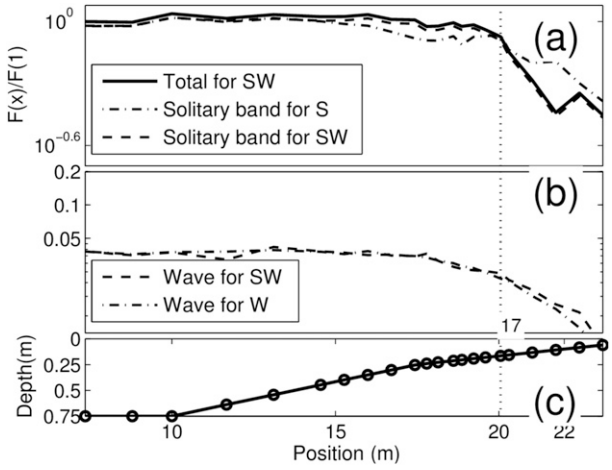

FIG. 8. Evolution of band energy flux (normalized by the total energy flux estimated at sensor 1) vs position for run SW4, the most nonlinear random wave run. (a) Total band for SW4 and solitary wave band for S and SW4; (b) random wave band for SW4 and W4. The solitary wave and random wave bands are defined in the time–frequency domain and divided using wavelet filter. The corresponding energy fluxes are calculated using Eqs. (2) and (3). (c) Bathymetry with the location of the sensors.

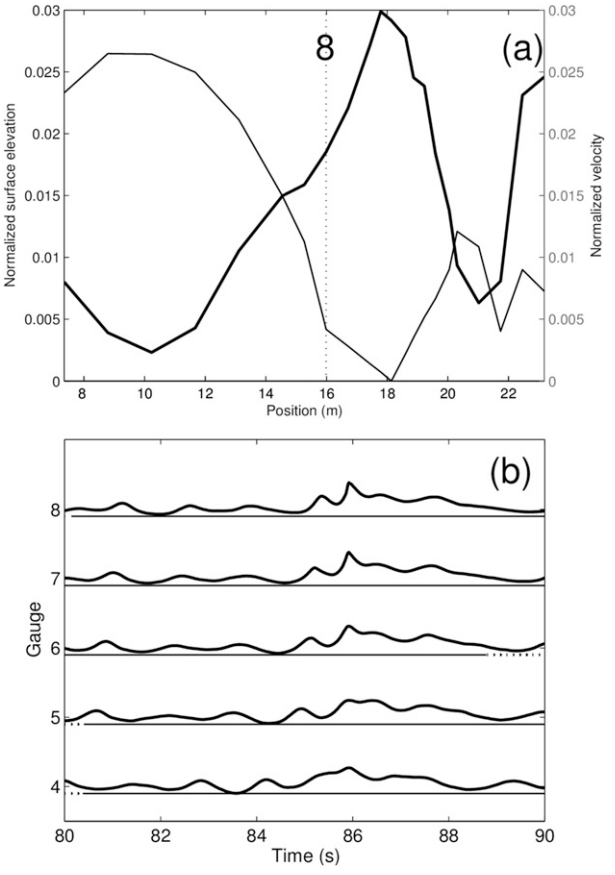

FIG. 9. Characteristic surface elevation, velocity, and phase of the seiche compared with the solitary wave characteristics for run SW3. (a) Amplitude of the surface elevation (thick line) and velocity (thin line), normalized by the local maximum amplitude and velocity of the solitary wave. The 8 represents gauge 8, where the solitary wave breaks for run SW3. (b) Surface elevation of the solitary wave (thick lines, arbitrary units) and direction of seiche flow (solid lines are shoreward; dashed lines are seaward) for the sensors in the vicinity of the breaking point.

expression in the evolution of the energy flux associated with the two wave fields. However, the evolution of net fluxes integrated over typical time–frequency bands (Fig. 8) does not show any significant energy exchange. Both waves are subject to breaking dissipation and the solitary wave flux decays faster in the presence of waves (Fig. 8a), but the evolution of the energy flux of the random waves shows no detectable change in the presence of the solitary wave (Fig. 8b). Note that in Fig. 8 the energy fluxes for S and SW4 represent one realization (30-s time series), while those for the random waves alone (run W4) are averaged for 47 realizations (12-min time series divided into 47 segments with 50% overlap). Therefore, discrepancies in the behavior of the two energy fluxes of the random waves are expected.

Tank seiching could also cause early breaking of the solitary wave and, if prominent, can affect the ability to translate these results to possible predictive applications. Approximating the seiche as a slowly varying current, we would anticipate that $U = O(c)$, where U and c are the characteristic velocities associated with the seiche and solitary wave, if the seiche were significant. If so, the modulation induced by the seiching should result in an increase in the frontal steepness for upstream propagation ($Uc < 0$) and thus early breaking. Defining the seiche domain in the estimated scalograms as $f < 0.05$ Hz (e.g., Figs. 4f–h), the surface elevation of the seiche can be determined from the measurements using the wavelet filter. Here, we are interested only in the seiche motion excited by the wave maker before the solitary wave runup and reflection on the slope. Elementary estimates of the seiche free-surface elevation and flow based on the linear approximation (e.g., Mellor 1996) indicate that 1) $U \ll c$ (Fig. 9a), and 2) in the runs available, the phase of the seiche is typically such that the solitary wave is stretched rather than compressed (Fig. 9b). The results suggest that the breaking of the solitary wave is not significantly influenced by the tank seiche.

b. *The effect of random waves*

The analysis of the previous section shows measurable effects of the random wave field on the solitary wave but without detectable conversion of energy to random C waves. The suppression of the growth of the solitary wave height suggests that the interaction could be

treated as a dissipative effect rather than a dynamical wave–wave interaction mechanism. In the presence of a random wave field, the nonlinear shoaling of the solitary wave may then be modeled using a variable coefficient-perturbed KdV equation (see the appendix):

$$\eta_t + c\eta_x + \frac{c_x}{2}\eta + \frac{3c}{2h}\eta\eta_x + \frac{ch^2}{6}\eta_{xxx} = -\frac{1}{2c}\mathscr{S}_x, \qquad (11)$$

where $\mathscr{S}$ is the radiation stresses due to the random wave field, and the subscripts denote derivatives (e.g., $\mathscr{S}_x$ is the gradient of the radiation stresses). With various forcing terms, this class of equations has been used extensively in the past to study the evolution of solitary waves over a sloping bed with forcing like bottom friction (e.g., Grimshaw 1979; Grimshaw et al. 2010, 2014; El et al. 2007; Johnson 1973a,b; and many others). In Eq. (11), the radiation stresses term on the right-hand side represents the forcing induced by the radiation stresses gradient. A similar equation was used by Grimshaw et al. (2014) to describe the combined effects of background rotation and variable topography on a slowly varying internal solitary wave. The slowly varying solitary wave solution yields for the evolution of the solitary wave height a (see the appendix)

$$a(x) = a_0\frac{h_0}{h(x)}[1 + D(x)], \quad \text{and} \qquad (12)$$

$$D(x) = \frac{\mathscr{S}_0 - \mathscr{S}(x)}{ga_0h_0}, \quad \mathscr{S} = \frac{gA^2}{2}\left(2\frac{C_g}{C} - \frac{1}{2}\right), \qquad (13)$$

where A, C, and C_g are the characteristic amplitude, phase, and group velocity of the random waves; a is the solitary wave amplitude; $\mathscr{S}(x)$ is the radiation stresses induced by short random waves; D is the dissipation rate; and the zero subscript denotes the value of the parameter at $x = x_0$. Equation (12) represents the shoaling law for the solitary wave. The effect of the random waves on the solitary wave is contained in the coefficient D.

Without random waves ($D = 0$) in Eq. (12), the solitary wave height increases monotonically as the water depth decreases. For the solitary wave, shoaling over undisturbed water, the evolution estimated based on Eq. (12) agrees well with observations (run S, the thin line in Fig. 10a). The observations exhibit the two-stage shoaling process identified by Synolakis (1991) and Synolakis and Skjelbreia (1993): (i) a standard Green's law stage, characterized by $a \propto h^{-1/4}$, and (ii) a rapid shoaling regime, governed by the Boussinesq law $a \propto h^{-1}$ (e.g., Grimshaw 1971). The Boussinesq law is a special case of Eq. (12) in which $D = 0$ and the solitary wave is infinitesimal.

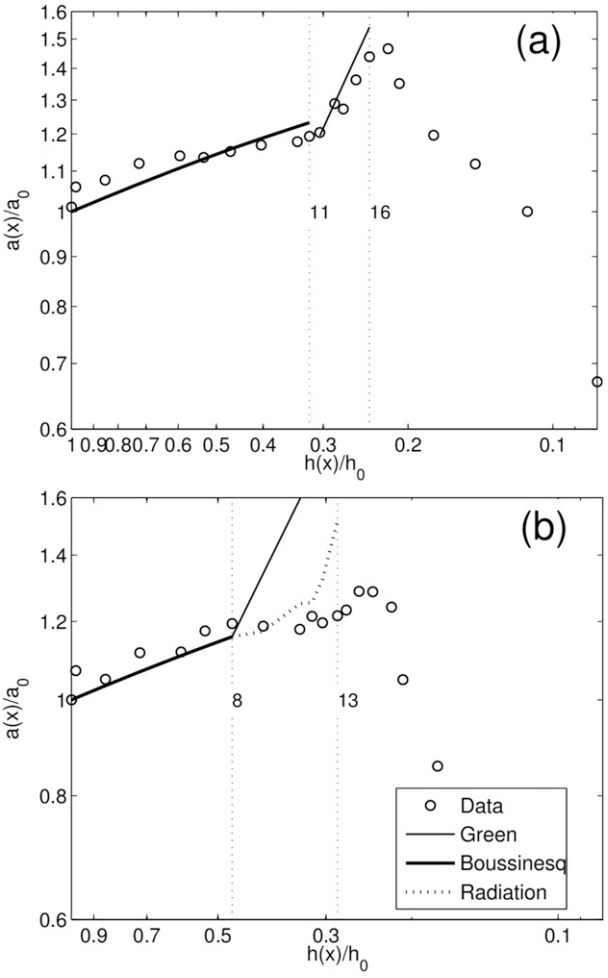

FIG. 10. Normalized solitary wave amplitude $a(x)/a_0$ vs normalized depth $h(x)/h_0$. (a) Solitary wave over undisturbed water (run S); (b) solitary wave in the presence of random waves run SW4. Dots indicate observations; thick lines indicate Green's law; thin lines indicate Boussinesq's law; and dashed lines indicate KdV shoaling with radiation stress [Eq. (A12)]. All SW runs exhibit a behavior similar to run SW4. Vertical dashed lines mark the boundaries of the Boussinesq-type shoaling domain.

In the presence of random waves, the variable radiation stress gradient modulates the behavior of the solitary wave. In the random wave shoaling zone, $\mathscr{S}_0 - \mathscr{S}(x) \le 0$; therefore, $D < 0$, and the radiation stress gradient acts as a dissipative force to suppress the solitary wave growth. After short waves break on the upper slope, $\mathscr{S}_0 - \mathscr{S}(x) > 0$, and the radiation stress gradient causes the solitary wave to grow, which may explain the early solitary wave breaking.

One can estimate the dissipation rate induced by the random waves using the 12-min runs of random waves only (run W4). The results based on Eq. (12), shown in Fig. 10b, appear to capture the trend of the observations despite the crudeness of the formulation (e.g., the

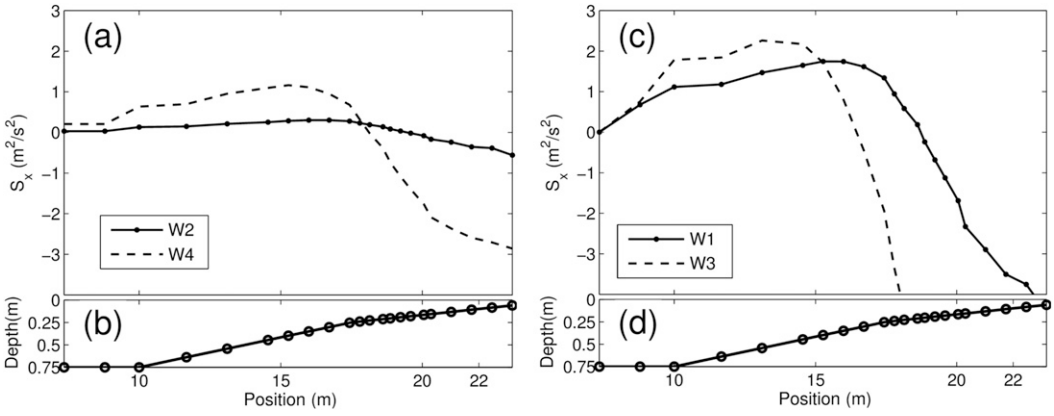

FIG. 11. Radiation stresses gradient vs position estimated using runs W for random waves alone, which consists of 47 realizations. (a),(c) Evolution of radiation stresses gradient; (b),(d) bathymetry with the location of the sensors. Dotted lines show runs W1 and W2; dashed lines show runs W3 and W4.

solitary wave is assumed to remain symmetric in the process) and the different statistics represented by the different curves. An alternative model not accounting for the dissipation induced by random waves (e.g., Synolakis and Skjelbreia 1993) significantly overestimates the shoaling growth rate.

The effect of the radiation stresses also explains the difference between the evolution of the solitary wave height in four SW runs (Fig. 7). Indeed, the height growth is weaker and breaking occurs earlier for runs SW1 and SW3, which exhibit a stronger radiation stresses gradient (Fig. 11b). Conversely, for a weak radiation stresses gradient, the effect of the random wave field on the solitary wave is also weak (Fig. 11a).

4. Numerical simulations

The early breaking phenomenon exhibited by all SW runs has so far been implicitly treated as statistically significant behavior, despite having only a single realization for each of the four runs. To overcome the scarcity of laboratory observations, we turn to a numerical model to simulate a statistical ensemble of runs. The numerical simulations were conducted using the Non-Hydrostatic WAVE model (NHWAVE) (Ma et al. 2012), a time-domain model capable of accurately describing fully dispersive, nonlinear surface waves in 3D coastal environments, as well as the breaking solitary wave runup and rundown on sloping beaches. The model solves the incompressible Navier–Stokes equations in well-balanced conservative form, with the governing equations discretized by a combined finite volume/finite difference approach with a Godunov-type shock-capturing scheme.

Numerical experiments were conducted using a 10-layer, $\Delta x = 0.03$-m grid resolution and an initial time step of $\Delta t = 0.02$ s (the time step is adjusted during computations based on the CFL number). The model used the topography of the laboratory experiment (Fig. 1), with the internal wave maker located at $x = 2.10$ m inside the domain, generating the time series measured at sensor 1. The simulations compare well with the observed time series (Fig. 12). They do not reproduce accurately the inundation induced by the solitary wave and its subsequent reflection; however, these processes are not of interest for this analysis. Although estimators of steepness based on the numerical simulations are less accurate, the essential trends (two major breaking events can be observed, while the first one occurs in relatively deeper water for all SW runs) of the observations are captured (Figs. 13–14).

For each of the four SW runs, an ensemble of 60 realizations was simulated by superposing the time series recorded at sensor 1 in run S with a random wave field constructed based on the random-phase approximation (random, uniformly distributed initial phases; e.g., Nazarenko 2011) to match the properties in Table 1. The statistical distribution of the solitary wave-breaking point (Fig. 15), obtained by applying the procedure detailed in sections 2–3, clearly shows the early breaking effect induced by the presence of the random wave field, with 93%, 72%, 100%, and 73% of the runs breaking earlier in simulations that reproduce runs SW1 to SW4, respectively.

5. Discussion and conclusions

Overhead video from a small number of laboratory experiments conducted by Kaihatu and El Safty (2011) and Kaihatu et al. (2012) at the Tsunami Wave Basin at Oregon State University suggests that the breaking

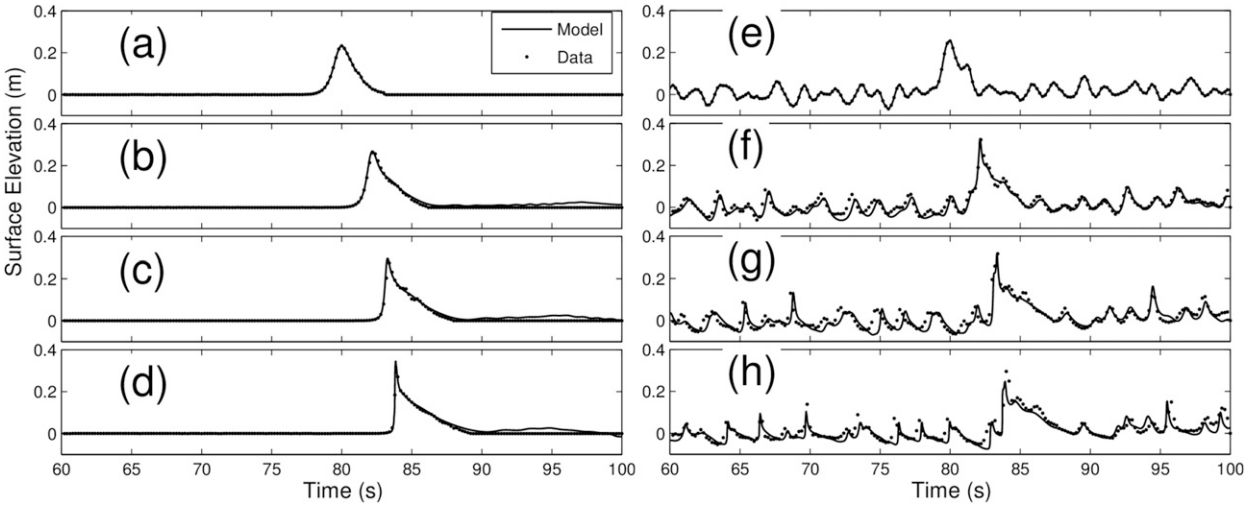

FIG. 12. Comparison between modeled and measured free-surface elevation for (a)–(d) run S and (e)–(h) run SW3 at gauges (top to bottom) 1, 6, 11, and 16. Lines indicate model results; dots indicate laboratory observations.

point of the solitary wave shifts to deeper water if random wave fields are present. In general, this points to the possibility of a measurable interaction between shoaling solitary waves and the background short-wave fields. The mechanism for this interaction has not been studied. By extension, in as much as the solitary wave can be used as a paradigm for tsunami propagation, one would hypothesize that a similar effect should be detectable in the case of shoaling tsunamis.

Understanding the evidence provided by the laboratory experiments posed a number of challenges. Surface elevation data were collected for only a small number of tests, and the early breaking of the solitary wave was established through visual inspection. The goal of this study was to quantify the perception of ''early breaking''; to verify the plausibility of this process; to develop a theoretical background for understanding the process; and finally to reconstruct the missing statistics to test the significance of the process.

Because of experimental constraints, the breaking criterion had to be formulated in terms of surface elevation evolution. The instantaneous breaking point was defined as the position corresponding to the solitary-wave slope reaching a maximum value (defined both as an average and a local value). For combined solitary wave/random wave runs, an additional difficulty was posed by the need to separate the solitary wave from the random wave signal. This difficulty was overcome by using a filter based on the time–frequency analysis (wavelet transform). The solitary wave signal was reconstructed by identifying its signature in the time–frequency domain and then reconstructing the time-domain signal using

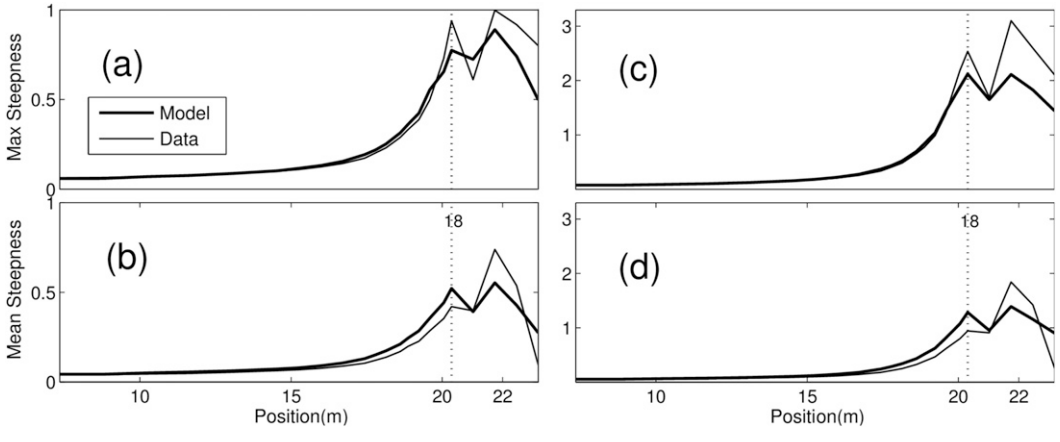

FIG. 13. Evolution of the frontal steepness for run S from model results and laboratory data. (a),(b) Nonlinear and (c),(d) linear estimations. (top) The maximum steepness; (bottom) the mean steepness. Dashed lines together with the text show the breaking location.

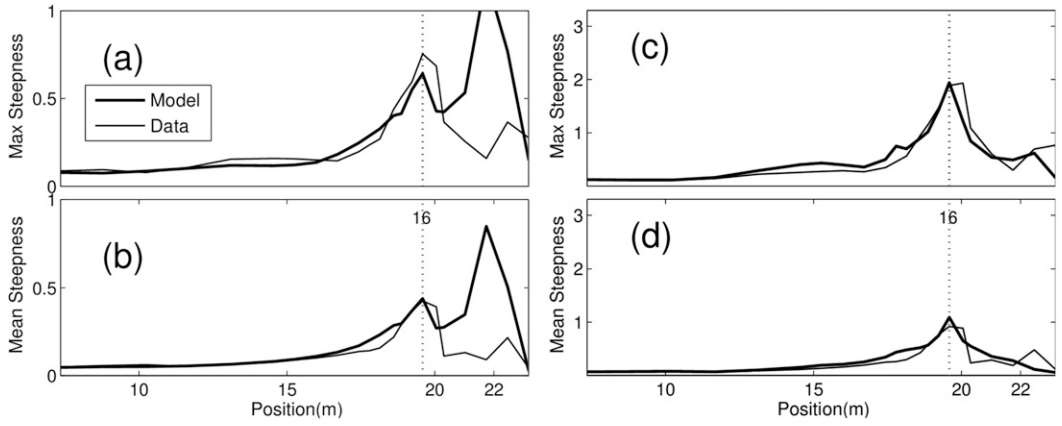

FIG. 14. As in Fig. 13, but for run SW4.

the inverse wavelet transform. The filtered data preserved the slope and peak of the solitary wave well enough to allow for estimating the frontal steepness even in the presence of the random waves.

The analysis based on the evolution of the maximum and mean steepness estimates confirms the visual observations (Kaihatu and El Safty 2011; Kaihatu et al. 2012). Moreover, it suggests that early breaking is accompanied by a suppressed amplitude growth. While breaking is clearly identifiable in the evolution of the energy fluxes associated with the solitary wave and the random waves, there is little evidence of a transfer of energy between them. The breaking process appears to have more in common with the process of wave

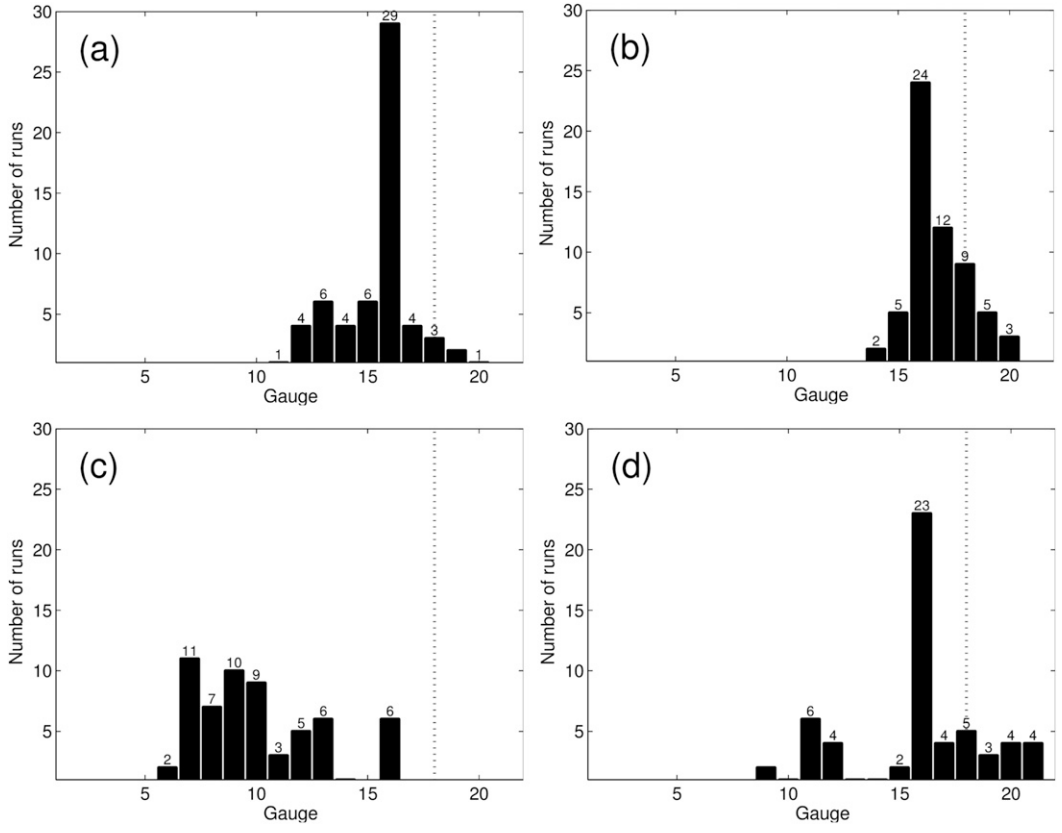

FIG. 15. Frequency of occurrence of solitary wave breaking estimated based on first maximum steepness at the locations of the sensors (total number of runs is 60). Dashed lines show the breaking location of the solitary wave propagating over undisturbed water (run S): (a) run SW1, (b) run SW2, (c) run SW3, and (d) run SW4.

propagation through a random flow perturbation than with wave–wave interaction processes. Indeed, a simple modification of the KdV model to include the radiation stresses forcing due to the random wave field compares well with the observed behavior of the solitary wave and explains differences between the four runs based on the characteristics of the random wave fields alone. The tank seiching was shown to be negligible for the solitary wave. The statistical ensemble, reconstructed using the NHWAVE model, confirms the significance of the random wave effect on the solitary wave shoaling.

We believe that the results of this study point to a potentially significant oceanographic process that has so far been ignored. They suggest that systematic research into the interaction between tsunami waves in their various realizations [N-waves in Tadepalli and Synolakis (1994); soliton fission in Madsen and Mei (1969); undular bores in Grue et al. (2008); etc.] is necessary for increasing the accuracy of tsunami forecasting. Laboratory experiments that further investigate this interaction, at a larger scale, are presently underway.

Acknowledgments. The experimental work was funded by NSF CMMI Grant 0936579 entitled "NEESR Payload: Determining the Added Hazard Potential of Tsunamis by Interaction with Ocean Swell and Wind Waves." Thanks go to the staff of the NEES Tsunami Wave Basin at Oregon State University; to Dr. Sungwon Shin, Tim Maddux, and Dan Cox; and to Ms. Melora Park, Ms. Linda Frayler, Mr. Jason Killian, and Mr. Adam Ryan. Thanks to Hoda El Safty, Brianna Schilling, Kyle Outten, and Belynda Alonzo (all at Texas A&M University at the time of the experiment) for their assistance in designing the experiment and in processing the data in a manner that helped facilitate their use for this study. We thank Dongyu Feng particularly for his generous help.

The data analysis effort (Drs. Tian and Sheremet) was supported by NSF Grant CMMI-120814, "Interaction of Tsunamis with Short Waves and Bottom Sediment—Numerical and Physical Modeling."

We are grateful to the anonymous reviewers for their advice in correcting errors in the initial KdV formulation of the solitary wave dissipation induced by the random waves.

APPENDIX

The KdV Equation with Radiation Stresses Forcing

Here, we present a formulation for the effect of random waves on solitary wave propagation based on the conceptual model of a wave propagating through a random flow, turbulent background. Because this is a fundamentally statistic model, the derivation presented below is not rigorous, the model will be applied eventually to a handful of realizations, and laboratory scaling may or may not be meaningful for field applications, we regard this model as a first, crude step toward understanding this process. Obviously, further work is required to establish a consistent theoretical model.

The goal of the approach is to modify the variable depth Korteweg–deVries equation (e.g., Grimshaw et al. 2010) to introduce the effect of the random waves as a radiation stress type of forcing. The linear shoaling of a long wave in the presence of short waves is governed by the second-order equation (e.g., Longuet-Higgins and Stewart 1962; Mei et al. 2005):

$$\eta_{tt} - (gh\eta_x)_x = -\mathscr{S}_{xx}, \tag{A1}$$

where x is the position, t is the time, $\eta(x, t)$ is the free-surface elevation, $h(x)$ is the depth, g is the gravitational acceleration, and $\mathscr{S}(x, t)$ is the radiation stress due to the random wave field. Subscripts x and t denote partial derivatives; for example, $\mathscr{S}_x$ is the radiation stress gradient.

The random wave field is assumed stationary and narrow spectrum, for example, $A_t = 0$, with $\mathscr{S}$ approximately given as

$$\mathscr{S} = \frac{gA^2}{2}\left(2\frac{C_g}{C} - \frac{1}{2}\right), \tag{A2}$$

where A, C, and C_g are the characteristic amplitude, phase, and group velocity of the random waves.

For the solitary wave, following Grimshaw (1971) and Grimshaw et al. (2010), we introduce the slow variables

$$X = \varepsilon x, \quad \xi = \varepsilon^2 x, \quad \text{and} \quad T = \varepsilon t,$$

where $h/L = \varepsilon \ll 1$ and $a/h \sim O(\varepsilon^2)$, with L and a characteristic spatial scale and height, and transform to a new reference frame moving with the velocity $c = \sqrt{gh(\xi)}$:

$$\tau = \frac{1}{\varepsilon^2}\int_0^{\xi} \frac{ds}{c(s)} - T. \tag{A3}$$

The free-surface elevation is assumed to scale as $\eta = \varepsilon^2\tilde{\eta}(\tau, \xi) + O(\varepsilon^4)$, with $\tilde{\eta} = O(1)$. In the new variables (τ, ξ), Eq. (A1) becomes

$$\varepsilon^6 2c\tilde{\eta}_{\tau\xi} + \varepsilon^6 c_\xi \tilde{\eta}_\tau + \varepsilon^8 (c^2\tilde{\eta}_\xi)_\xi = -\varepsilon^2 \mathscr{S}_{\tau\tau} + O(\varepsilon^8). \tag{A4}$$

Neglecting the terms of order $O(\varepsilon^8)$, integrating once over τ, and reverting to the original coordinates finally yields the equation

$$\eta_t + c\eta_x + \frac{c_x}{2}\eta = -\frac{1}{2c}\mathscr{S}_x. \tag{A5}$$

Note that the magnitude of $\mathscr{S}$ has not been discussed so far. To be included into Eq. (A5), $\mathscr{S}$ should be scaled as $\mathscr{S}_{xx} = O(\varepsilon^6)$, which implies that either $\mathscr{S}(X)$ and $A/h = O(\varepsilon^2)$ or $\mathscr{S}(x)$ and $A/h = O(\varepsilon^3)$. For our experiment, the former seems more suitable, as the random waves are of the same order of magnitude as the solitary wave. Equation (A7) can be put in the equivalent form

$$\eta_x = -\frac{1}{c}\left(\eta_t + \frac{c_x}{2}\eta + \frac{1}{2c}\mathscr{S}_x\right). \tag{A6}$$

For shoaling random waves $\mathscr{S}_x > 0$; therefore, the radiation stress term in Eq. (A6) increases the long-wave frontal steepness, accelerating breaking.

The nonlinear terms can now be accounted for by using the variable coefficient KdV equation (e.g., Grimshaw 1971, 1979; Johnson 1973a,b):

$$\eta_t + c\eta_x + \frac{c_x}{2}\eta + \frac{3c}{2h}\eta\eta_x + \frac{ch^2}{6}\eta_{xxx} = -\frac{1}{2c}\mathscr{S}_x. \tag{A7}$$

Switching spatial to time derivatives, for example, $\eta_t = -c\eta_x + O(\varepsilon^4)$, Eq. (A7) can be written in a more convenient form for our experimental framework:

$$\eta_t + c\eta_x + \frac{c_x}{2}\eta - \frac{3}{2h}\eta\eta_t - \frac{h^2}{6c^2}\eta_{ttt} = -\frac{1}{2c}\mathscr{S}_x. \tag{A8}$$

A conservation law for Eq. (A8) is

$$\frac{\partial}{\partial x}\int_{-\infty}^{\infty} c\eta^2\, dt = -\int_{-\infty}^{\infty}\frac{1}{c}\eta\mathscr{S}_x\, dt. \tag{A9}$$

Both Eqs. (A7) and (A8) have a slowly varying solitary wave solution for η at the leading order (e.g., Grimshaw 1971, 1979; Grimshaw et al. 2010, 2014):

$$\eta = a\,\mathrm{sech}^2[k(x - Vt)], \quad k = \left(\frac{3a}{4h^3}\right)^{1/2}, \quad V = c + \frac{ca}{2h}. \tag{A10}$$

Substituting Eq. (A10) into Eq. (A9) yields for Eq. (A9) the form

$$[(ah)^{3/2}]_x = -\frac{3\mathscr{S}_x}{2g}(ah)^{1/2}. \tag{A11}$$

Equation (A11) can be readily integrated to yield

$$a(x) = a_0\frac{h_0}{h(x)}[1 + D(x)], \quad \text{and} \tag{A12}$$

$$D(x) = \frac{\mathscr{S}_0 - \mathscr{S}(x)}{ga_0h_0}, \tag{A13}$$

where $h_0 = h(x_0)$ and $\mathscr{S}_0 = \mathscr{S}(x_0)$ are the initial depth and radiation stresses at $x = x_0$.

REFERENCES

Aida, I., K. Kajiura, T. Hatori, and T. Momoi, 1964: A tsunami accompanying the Niigata earthquake of June 16, 1964 (in Japanese). *Bull. Earthquake Res. Inst. Univ. Tokyo,* **42,** 741–780.

Bouws, E., H. Gunther, W. Rosenthal, and C. L. Vincent, 1985: Similarity of the wind spectrum in finite depth water: 1. Spectral form. *J. Geophys. Res.,* **90,** 975–986, doi:10.1029/JC090iC01p00975.

Chui, C. K., 1992: *An Introduction to Wavelet: Wavelet Analysis and Its Applications.* Academic Press, 264 pp.

Constantin, A., and R. Johnson, 2008: Propagation of very long water waves with vorticity over variable depth with applications to tsunamis. *Fluid Dyn. Res.,* **40,** 175–211, doi:10.1016/j.fluiddyn.2007.06.004.

El, G., R. Grimshaw, and A. Kamchatnov, 2007: Evolution of solitary waves and undular bores in shallow-water flows over a gradual slope with bottom friction. *J. Fluid Mech.,* **585,** 213–244, doi:10.1017/S0022112007006817.

Farge, M., 1992: Wavelet transforms and their applications to turbulence. *Annu. Rev. Fluid Mech.,* **24,** 395–457, doi:10.1146/annurev.fl.24.010192.002143.

Fritz, H. M., and Coauthors, 2012: The 2011 Japan tsunami current velocity measurements from survivor videos at Kesennuma Bay using LiDAR. *Geophys. Res. Lett.,* **39,** L00G23, doi:10.1029/2011GL050686.

Geist, E., V. Titov, and C. Synolakis, 2006: Tsunami: Wave of change. *Sci. Amer.,* **294,** 56–63, doi:10.1038/scientificamerican0106-56.

Goring, D. G., 1979: Tsunamis—The propagation of long waves onto a shelf. W. M. Keck Laboratory of Hydraulics and Water Resources, California Institute of Technology, Rep. KH-R-38, 356 pp.

Goupillaud, P., P. A. Grossman, and J. Morlet, 1984: Cycle-octave and related transforms in seismic signal analysis. *Geoexploration,* **23,** 85–102, doi:10.1016/0016-7142(84)90025-5.

Grilli, S. T., S. Vogelmann, and P. Watts, 2002: Development of a 3D numerical wave tank for modeling tsunami generation by underwater landslides. *Eng. Anal. Boundary Elem.,* **26,** 301–313, doi:10.1016/S0955-7997(01)00113-8.

Grimshaw, R., 1971: The solitary wave in water of variable depth. Part 2. *J. Fluid Mech.,* **46,** 611–622, doi:10.1017/S0022112071000739.

——, 1979: Slowly varying solitary waves. I. Korteweg-de Vries equation. *Proc. Roy. Soc. London,* **A368,** 359–375, doi:10.1098/rspa.1979.0135.

——, E. Pelinovsky, T. Talipova, and O. Kurkina, 2010: Internal solitary waves: Propagation, deformation and disintegration. *Nonlinear Processes Geophys.,* **17,** 633–649, doi:10.5194/npg-17-633-2010.

——, C. Guo, K. Helfrich, and V. Vlasenko, 2014: Combined effect of rotation and topography on shoaling oceanic internal solitary waves. *J. Phys. Oceanogr.,* **44,** 1116–1132, doi:10.1175/JPO-D-13-0194.1.

Grue, J., E. N. Pelinovsky, D. Fructus, T. Talipova, and C. Kharif, 2008: Formation of undular bores and solitary waves in the Strait of Malacca caused by the 26 December 2004 Indian Ocean tsunami. *J. Geophys. Res.,* **113,** C05008, doi:10.1029/2007JC004343.

Ippen, A. T., and G. Kulin, 1954: The shoaling and breaking of the solitary waves. *Proc. Fifth Int. Conf. on Coastal Engineering,* New York, NY, ASCE, 27–47.

Johnson, R. S., 1973a: On the development of a solitary wave moving over an uneven bottom. *Math. Proc. Cambridge Philos. Soc.,* **73,** 183–203, doi:10.1017/S0305004100047605.

——, 1973b: On an asymptotic solution of the Korteweg–de Vries equation with slowly varying coefficients. *J. Fluid Mech.,* **60,** 813–824, doi:10.1017/S0022112073000492.

Kaihatu, J. M., and H. M. El Safty, 2011: The interaction of tsunamis with ocean swell: An experimental study. *Proc. 30th Int. Conf. on Ocean, Offshore and Arctic Engineering,* Rotterdam, Netherlands, ASME, 747–754, doi:10.1115/OMAE2011-49936.

——, D. Devery, R. J. Erwin, and J. T. Goertz, 2012: The interaction between short ocean swell and transient long waves: Dissipative and nonlinear effects. *Proc. 33rd Conf. on Coastal Engineering,* Santander, Spain, ASCE, wave.20. [Available online at https://journals.tdl.org/icce/index.php/icce/article/view/7012.]

Kowalik, Z., T. Proshutinsky, and A. Proshutinsky, 2006: Tide-tsunami interactions. *Sci. Tsunami Hazards,* **24,** 242–256. [Available online at http://tsunamisociety.org/244kowalik.pdf.]

Longuet-Higgins, S., 1987: The propagation of short surface waves on longer gravity waves. *J. Fluid Mech.,* **177,** 293–306, doi:10.1017/S002211208700096X.

——, and R. Stewart, 1962: Radiation stress and mass transport in gravity waves with application to surf beats. *J. Fluid Mech.,* **13,** 481–504, doi:10.1017/S0022112062000877.

Ma, G.-F., F. Shi, and J. T. Kirby, 2012: Shock-capturing non-hydrostatic model for fully dispersive surface wave processes. *Ocean Modell.,* **43–44,** 22–35, doi:10.1016/j.ocemod.2011.12.002.

Madsen, O. S., and C. C. Mei, 1969: The transformation of a solitary wave over an uneven bottom. *J. Fluid Mech.,* **39,** 781–791, doi:10.1017/S0022112069002461.

Madsen, P. A., D. R. Fuhrman, and H. A. Schäffer, 2008: On the solitary wave paradigm for tsunamis. *J. Geophys. Res.,* **113,** C12012, doi:10.1029/2008JC004932.

Matsuyama, M., M. Ikeno, T. Sakakiyama, and T. Takeda, 2007: A study of tsunami wave fission in an undistorted experiment. *Pure Appl. Geophys.,* **164,** 617–631, doi:10.1007/s00024-006-0177-0.

Mei, C. C., M. Stiassnie, and D.-P. Yue, 2005: *Theory and Applications of Ocean Surface Waves.* Advanced Series on Ocean Engineering, Vol. 23, World Scientific, 1136 pp.

Mellor, G. L., 1996: *Introduction to Physical Oceanography.* American Institute of Physics, 260 pp.

Nazarenko, S., 2011: *Wave Turbulence.* Lecture Notes in Physics, Vol. 825, Springer, 279 pp.

Osborne, A. R., 2010: *Nonlinear Ocean Waves and the Inverse Scattering Transform.* International Geophysics Series, Vol. 97, Academic Press, 944 pp.

Peregrine, D. H., 1983: Breaking waves on beaches. *Annu. Rev. Fluid Mech.,* **15,** 149–178, doi:10.1146/annurev.fl.15.010183.001053.

Synolakis, C. E., 1991: Green's law and the evolution of solitary waves. *Phys. Fluids,* **3A,** 490–491, doi:10.1063/1.858107.

——, and J. E. Skjelbreia, 1993: Evolution of maximum amplitude of solitary waves on plane beaches. *J. Waterw. Port Coastal Ocean Eng.,* **119,** 323–342, doi:10.1061/(ASCE)0733-950X(1993)119:3(323).

Tadepalli, S., and C. Synolakis, 1994: The run-up of N-waves on sloping beaches. *Proc. Roy. Soc. London,* **A445,** 99–112, doi:10.1098/rspa.1994.0050.

Torrence, C., and G. P. Compo, 1998: A practical guide to wavelet analysis. *Bull. Amer. Meteor. Soc.,* **79,** 61–78, doi:10.1175/1520-0477(1998)079<0061:APGTWA>2.0.CO;2.

Whitham, G. B., 1974: *Linear and Nonlinear Waves.* Pure and Applied Mathematics Series, Wiley, 636 pp.

Zhang, J., and W. K. Melville, 1990: Evolution of weakly nonlinear short waves riding on long gravity waves. *J. Fluid Mech.,* **214,** 321–346, doi:10.1017/S0022112090000155.